iScience

CellPress
OPEN ACCESS

Article

Quantifying cell-cycle-dependent chromatin dynamics during interphase by live 3D tracking

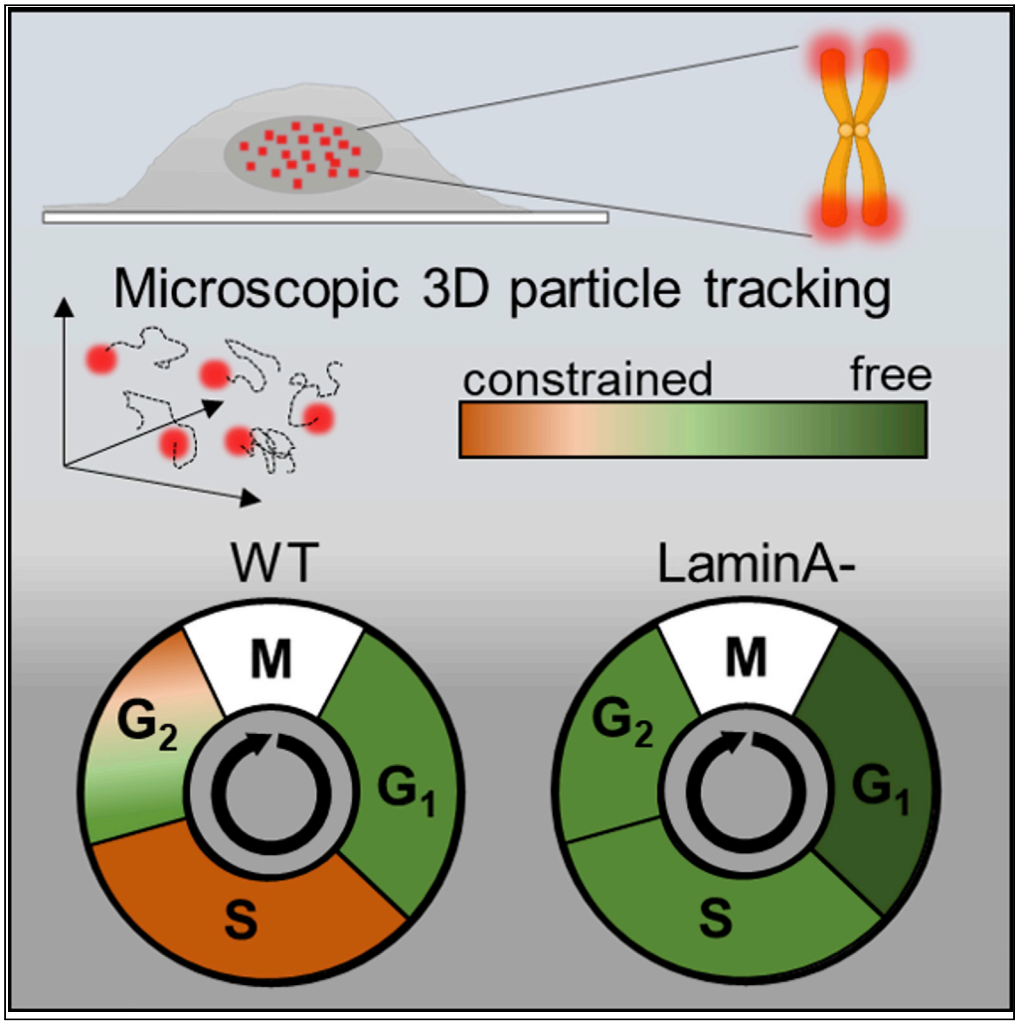

Tal Naor, Yevgeni Nogin, Elias Nehme, Boris Ferdman, Lucien E. Weiss, Onit Alalouf, Yoav Shechtman

yoavsh@technion.ac.il

Highlights

PSF engineering allows scan-free, high spatiotemporal live 3D telomere tracking

During the G0/G1 phase, telomere motion is less constrained than in other phases

There is observable difference between lateral (xy) and axial (z) chromatin motion

In Lamin A-depleted cells, motion constraint was reduced

Naor et al., iScience 25, 104197
May 20, 2022
https://doi.org/10.1016/j.isci.2022.104197

iScience

CellPress
OPEN ACCESS

Article

Quantifying cell-cycle-dependent chromatin dynamics during interphase by live 3D tracking

Tal Naor,[1] Yevgeni Nogin,[1,2] Elias Nehme,[1,3] Boris Ferdman,[1,2] Lucien E. Weiss,[1,4] Onit Alalouf,[1] and Yoav Shechtman[1,2,5,*]

SUMMARY

The study of cell cycle progression and regulation is important to our understanding of fundamental biophysics, aging, and disease mechanisms. Local chromatin movements are generally considered to be constrained and relatively consistent during all interphase stages, although recent advances in our understanding of genome organization challenge this claim. Here, we use high spatiotemporal resolution, 4D (x, y, z and time) localization microscopy by point-spread-function (PSF) engineering and deep learning-based image analysis, for live imaging of *mouse embryonic fibroblast* (MEF 3T3) and MEF 3T3 double Lamin A Knockout (LmnaKO) cell lines, to characterize telomere diffusion during the interphase. We detected varying constraint levels imposed on chromatin, which are prominently decreased during G0/G1. Our 4D measurements of telomere diffusion offer an effective method to investigate chromatin dynamics and reveal cell-cycle-dependent motion constraints, which may be caused by various cellular processes.

INTRODUCTION

There has been a growing interest in 3D genome organization and dynamics in recent years (Maeshima et al., 2020). The basic structure, namely the 10 nm chromatin fiber, is composed of DNA wrapped around a histone core to form nucleosomes which are separated by non-nucleosome linker DNA and other DNA-binding proteins. This current model for genome organization has been refined using different high-resolution methods, including cryo-EM tomography (Eltsov et al., 2008; Cai et al., 2018), X-ray scattering (Nishino et al., 2012), super-resolution microscopy (STORM and PALM) (Ricci et al., 2015; Nozaki et al., 2017), and genomic methods (Lieberman-Aiden et al., 2009; Hsieh et al., 2015; Sanborn et al., 2015; Ohno et al., 2019). The clustering of nucleosomes to form domains (Sanborn et al., 2015; Nozaki et al., 2017), which vary in size and shape (Ricci et al., 2015; Maeshima et al., 2020; Lin et al., 2021), is a dynamic process (Bintu et al., 2018). The biophysical properties of the domains were extensively investigated, and include condensate formation, possibly by liquid-liquid phase separation (Banani et al., 2017; Strom et al., 2017; Gibson et al., 2019; Sanulli et al., 2019; Lee et al., 2020), leading to local isolated environments. The clustering of several domains into transcriptionally active compartments (euchromatin) and generally silent compartments (heterochromatin) (Lieberman-Aiden et al., 2009) makes up the chromosome that occupies a distinct volume in the nucleus, namely a chromosome territory (Maeshima et al., 2020).

Live-cell imaging and optical-field-correlation maps have revealed dynamic structural changes in Chromatin (Nozaki et al., 2017; Bintu et al., 2018; Shaban et al., 2020). Local chromatin (single domain) motion is generally constrained (subdiffusive); however, it can also exhibit Brownian-like (free) and active transport (superdiffusive) behaviors (Chuang et al., 2006; Bronshtein et al., 2015; Nozaki et al., 2017; Shaban et al., 2020), Figure 1B. The constrained dynamics of chromatin is explained by the necessity to preserve nucleus compartmentalization, which is maintained by the activity of several factors, such as cohesin (Liu et al., 2021), condensin, and lamins (Bronshtein et al., 2015; Narendra et al., 2015; Vivante et al., 2019; Karoutas and Akhtar, 2021), in particular nucleoplasm Lamin A. On the other hand, rapid turnovers of domain formation and

[1]Department of Biomedical Engineering and Lokey Interdisciplinary Center for Life Sciences & Engineering, Technion-IIT, Haifa, 3200003, Israel

[2]Russell Berrie Nanotechnology Institute, Technion-IIT, Haifa 3200003, Israel

[3]Department of Electrical Engineering, Technion-IIT, Haifa 3200003, Israel

[4]Department of Engineering Physics, Polytechnique Montréal, Montreal H3T 1J4, Quebec, Canada

[5]Lead contact

*Correspondence: yoavsh@technion.ac.il

https://doi.org/10.1016/j.isci.2022.104197

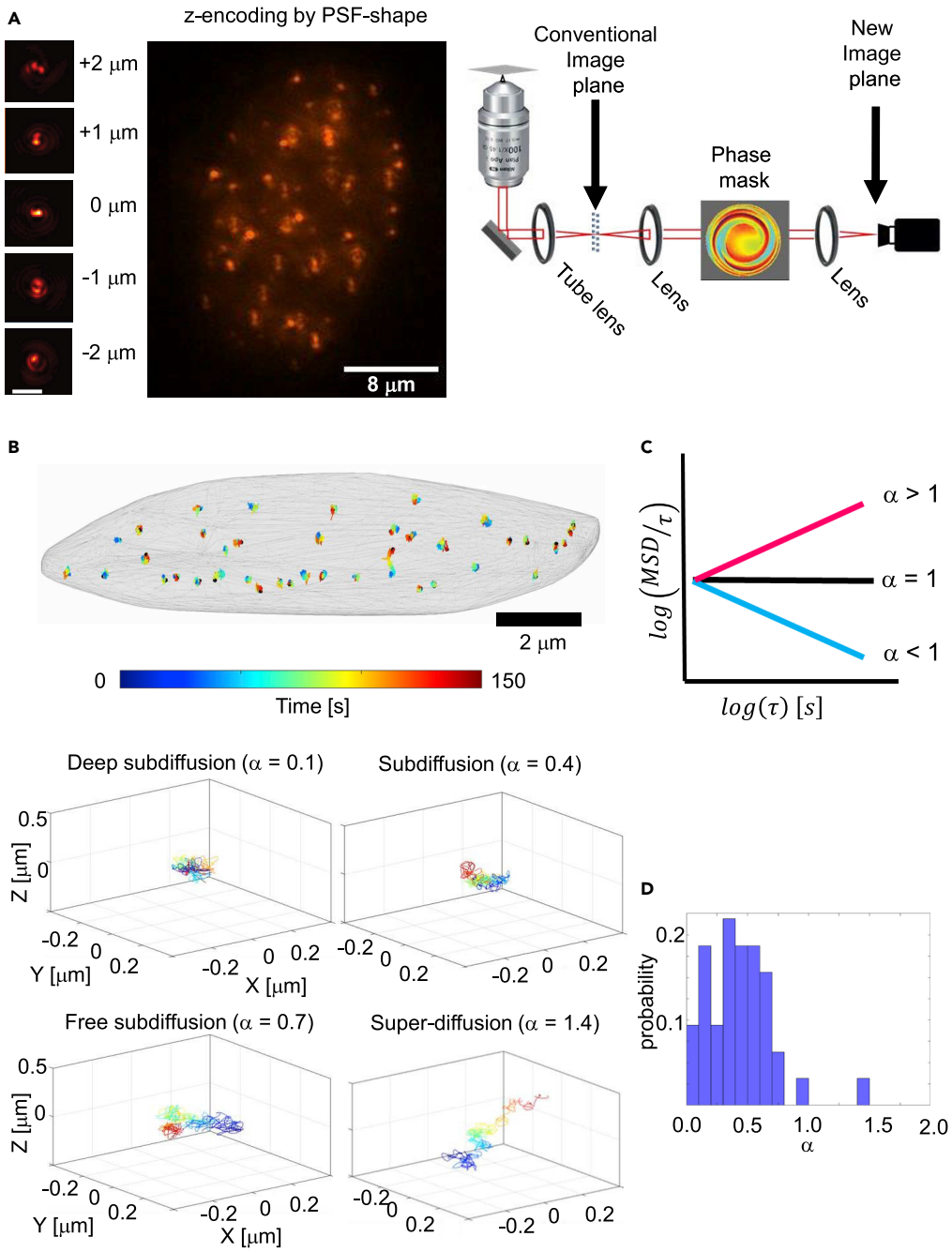

Figure 1. 3D telomere tracking in live cells using PSF engineering

(A) Example image of a live cell containing 3D information of labeled telomere positions using a depth-encoding phase mask in the microscope setup (right), more details in SI: Figure S1. The 3D position of each telomere is determined algorithmically according to an experimentally derived PSF model obtained from a calibration image stack of a defocused fluorescent bead (left, distance from the focal plane stated, scale bar = 3 μm).

(B) The trajectories of the telomeres are reconstructed from their localizations over time (four example telomeres are shown at the bottom). Color indicates time (See Video S1).

(C) Mean square displacement (MSD) analysis and the derived anomalous exponent (α) distinguishes between three main types of motion: subdiffusion (blue), normal diffusion (black), and super-diffusion (red).

(D) Anomalous exponent histogram of all detected telomeres (n = 38) in the cell shown in B.

disassembly (Bintu et al., 2018), as well as repositioning events (Levi et al., 2005; Albiez et al., 2006; Chowdhary et al., 2019; Fasciani et al., 2020) and transient compartment formation (Cisse et al., 2013; Furlong and Levine, 2018; Fasciani et al., 2020; Kim and Kingston, 2020), for example for transcription activation, and preparation for division, can contribute to more freely diffusing motion.

The cell cycle is a well regulated process that includes distinct phases: during gap 1 phase (G1) the cell increases in size, and then enters the synthesis phase (S) in which the genetic material is being replicated, followed by further cell expansion in gap 2 phase (G2), leading to the mitotic phase (M) where the cell divides (Humphrey and Brooks, 2005). Cell population in G1 may enter the resting phase (G0) (Da Silva-álvarez and Collado, 2018); when this phase is reversible, it is referred to as quiescent G0. For populations that include both G1 and quiescent G0 cells, the first phase of the interphase is referred to as G0/G1 (Hahn et al., 2009). While cell-cycle-dependent epigenetic mechanisms (Bui et al., 2012), such as protein-chromatin interactions, are well known, fundamental questions regarding chromosome dynamics during the interphase remain open. Earlier studies reported that local chromatin motion is similar throughout the different phases (G1/G0, S, and G2) (Nozaki et al., 2017); however, recent studies suggest otherwise: all-nucleus scale analysis reported different chromatin dynamics between G0 and G1 cells (Shaban et al., 2020), and single-locus analysis in U2OS shows that domains possibly undergo condensation-relaxation cycles during the transition from G1 to S and from S to G2 (Ma et al., 2019).

Fluorescence microscopy is used to directly observe chromatin in live cells (Weiss et al., 2018). However, conventional volumetric (3D) imaging is based on scanning (confocal or z stack), which limits the temporal and spatial resolutions of the microscope. Point-spread-function (PSF) engineering enables 3D imaging without scanning, achieving high frame rates. This is done by inserting a specially designed optical element, namely a phase mask, into the microscope. Emitted light from the sample is modulated by the phase mask such that its 3D information is encoded in the 2D image that a point emitter generates on the camera (the PSF). Then, using image analysis (Pavani et al., 2009; Backer and Moerner, 2014; Shechtman et al., 2015, 2017; Von Diezmann, Shechtman and Moerner, 2017), a precise 3D estimate of the emitter's position, i.e. a localization, is obtained (Figure 1A). This spatial encoding makes high densities of fluorescent molecules, where there is significant spatial overlap of PSFs, a challenging image processing problem of multi-emitter localization. Recently, our group introduced a deep learning-based method (DeepStorm3D (Nehme et al., 2020)), which we employ here, to handle dense-emitter samples, such as fluorescently labeled telomeres in the nucleus, enabling high spatiotemporal resolution in >50 positions in a single nucleus simultaneously. The method provides both the optimal phase-mask design and the accompanying image analysis algorithm (Nehme et al., 2020).

Here, we characterize cell-cycle-dependent telomere diffusion during the different interphase stages (G0/G1, S, G2, and late G2) in live *mouse embryonic fibroblast* (MEF 3T3) and MEF 3T3 double Lamin A Knockout (LmnaKO) cell lines, using 4D localization microscopy (x, y, z, and time) by PSF engineering combined with neural net-based image analysis (Nehme et al., 2020). Because telomeres are spread throughout the nucleus, our simultaneous measurement of multi-telomere diffusion represents local chromatin (single domain) movement across the genome. We report three key findings based on our observations: (1) The motion constraints normally imposed on chromatin are significantly relaxed during G0/G1 relative to the other stages in the cell cycle; (2) under Lamin A depletion, chromatin motion becomes more Brownian-like, irrespective of cell cycle phase, such that the observed differences are significantly reduced; and (3) the 3D motion of chromatin is anisotropic. This is possibly the result of the inherent anisotropy of adherent cells.

RESULTS AND DISCUSSION

To compare the motion of chromatin at different stages of the cell cycle, we tracked telomeres, labeled by DsRed-hTRF1 (see STAR Methods for details), in 3D with high spatiotemporal resolution (xy: ~20 nm;

z: ~50 nm; t: 10 Hz, see SI: Table S1). Prior to live-cell imaging, MEF 3T3 and MEF LmnaKO cells were synchronized to different phases in the cell cycle. To track the 3D positions at high frame rates, we engineered a PSF optimized for a depth range of 2–6 μm above the coverslip, which allows us to image a 4 μm Z section of nucleus without scanning. To extract the 3D trajectories, the raw images underwent a post-processing pipeline which includes frame-by-frame localization using DeepSTORM3D (Ferdman et al., 2020; Nehme et al., 2020), followed by reconstruction of telomere trajectories (telomere 3D positions over time, Figure 1B) using a custom python code (See SI: Figure S1 for analysis details). To characterize the dynamics of each population (cell cycle phases), we analyzed all the 3D trajectories from all cells for each phase separately, using mean square displacement (MSD, Figure 1C), which corresponds to the mean distance that a telomere will travel within a specific time interval (τ), ranging from 100 ms to 30 s.

We quantified chromatin motion for each phase using the following set of parameters: anomalous exponent (α), diffusion constant (D_α), and constraining volume (V_c). The anomalous exponent (α) defines the type of motion, as illustrated in Figure 1C, and is calculated for each trajectory from the slope of two linear fits of the MSD curve, corresponding to small intervals ($\tau < \tau_r$) and large intervals ($[\tau_L,\ 30\ s]$) (Figures 2A–2C). τ_r and τ_L represent transition times (De Gennes, 1971; Briels, 1998; Bronstein et al., 2009), where the ensemble MSD curve change trends from deep subdiffusion to moderate subdiffusion (See STAR Methods for precise definition of transition times). The diffusion constant ($D_\alpha\left[\mu m^2/_{s^\alpha}\right]$), associated with chromatin condensation (Ma et al., 2019; Shaban et al., 2020), is calculated from the independent variable of the MSD linear fit of the short time intervals, $t < \tau_r$. The constraining volume ($V_c[\mu m^3]$) is the mean volume that a telomere "explores" within 25 s, estimated by calculating the convex hull of each telomere trajectory (see STAR Methods).

Local chromatin 3D motion is less constrained during G0/G1 phase

Our first question is whether local chromatin movements manifest different dynamics during the different stages of the interphase. To do so, MEF 3T3 cells were synchronized in G0/G1, S, early G2, and late G2 phase and imaged for 150 s with 100 ms exposure time using the PSF-engineered microscope (cell cycle stage was verified by flow cytometry, see SI: Figure S3). Approximately 1,300 fluorescently labeled telomeres were tracked, several hundreds in each phase (see SI: Table S2). Trajectories were analyzed individually and the results were grouped by phase. We determined the level of constraint described by the anomalous exponent and distinguished between short and long time intervals. For the short times ($\tau < \tau_r$), no significant differences were observed between the phases ($\alpha \sim 0.2$, Figure 2B); while for longer timescales ($t \in [\tau_L, 30s]$), we identified different constraint levels (Figures 2A and 2B): deep subdiffusion during S, $\langle\alpha\rangle = 0.41 \pm 0.29$ and late G2, $\langle\alpha\rangle = 0.47 \pm 0.3$; moderate subdiffusion during early G2, $\langle\alpha\rangle = 0.59 \pm 0.32$; and free subdiffusion, $\langle\alpha\rangle = 0.83 \pm 0.34$ during G0/G1 (mean $\pm$ 1 std).

Our findings, which were performed on cells with a normal cell cycle over the entire nucleus, show that the 3D local chromatin motion varies during the interphase, consistent with the 2D single-chromosome analysis performed by Ma et al. (2019), which challenged the claim that chromosome motion is consistent during the interphase (Nozaki et al., 2017). Ma et al. tracked two loci on chromosome 19 in cancer cells with an abnormal cell cycle (U2OS), and showed that their centroid trajectories have a higher anomalous exponent in G1 compared to early S phase. In the current work, our conclusion about local chromatin motion is general: we find that telomere diffusion exhibits significant heterogeneity in terms of the anomalous exponent distribution even in the same cell (Figure 1B) (Bronshtein et al., 2015; Shaban et al., 2020); yet, overall, telomere diffusion is phase dependent (Figures 2A and 2B) in cells with a normal cell cycle.

To summarize, by calculating 3D telomere diffusion, we have found that different levels of constraint are imposed on the chromatin in different interphase stages; where the most constrained diffusion is observed during the S and late G2 phases, and the least constraint, i.e. least constrained diffusion dynamics are observed during the G0/G1.

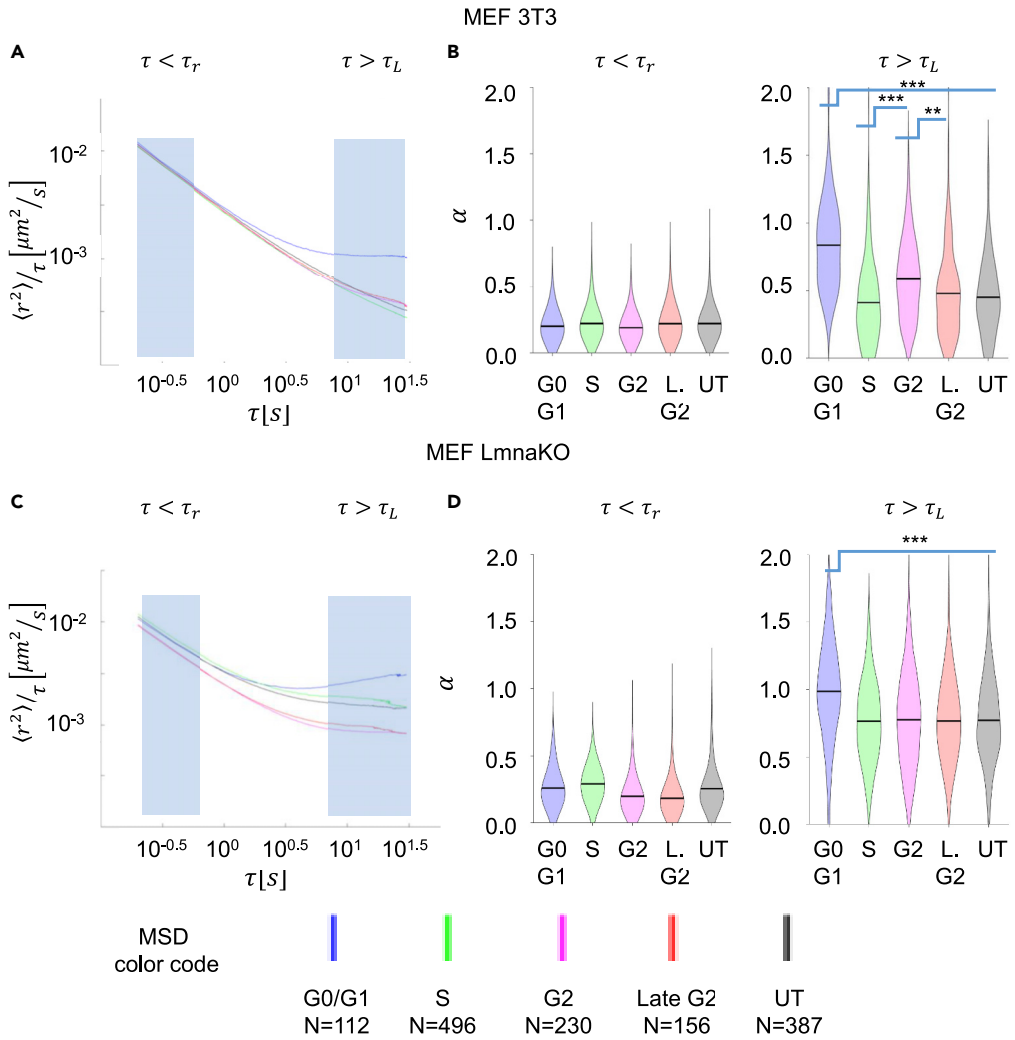

Figure 2. Telomere diffusion analysis in different cell cycle phases

Ensemble mean square displacement (MSD) curves and anomalous exponent (α) in MEF 3T3 (A, B) and in MEF LmnaKO (C, D) cells (see also Figure S3 for synchronization validation, and Table S2 for statistical parameters). α is represented as violin plots for short interval times ($t<\tau_r$) and long interval times ($t>\tau_L$). Shaded regions in (A, C) mark the short and long interval ranges analyzed for G0/G1. See all transition time values in SI: Table S2. UT – untreated cells. N is the number of trajectories analyzed in MEF 3T3. Confidence in two sample tests (See STAR Methods for details, and also Table S3): *p < 0.05, **p < 0.01, ***p < 0.001.

Lamin A depletion decreases constraint differences between cell cycle phases

Lamin A is a protein involved in maintaining the nuclear envelope integrity, protecting the genome from mechanical stress, and preserving nuclear compartmentalization (Johnson et al., 2004; Nitta et al., 2006; Scaffidi and Misteli, 2006; Nitta et al., 2007; Bronshtein et al., 2015; Shachar et al., 2015; Karoutas and Akhtar, 2021). In addition, a mutant cell line with double knockout of Lamin A, MEF LmnaKO cells, exhibits defective cell cycle regulation (Johnson et al., 2004; Nitta et al., 2006; Dechat et al., 2007; Nitta et al., 2007; Cho et al., 2019), as also indicated by our flow cytometry results (Figure S3). Furthermore, *MEF LmnaKO* cells are an important model for premature aging studies (Oshima et al., 2007; Ghosh and Zhou, 2014; Grigoryan et al., 2018). In light of the cell-cycle-dependent chromatin motion we observed in MEF 3T3 cells, we raised the question: does the function of Lamin A have an effect on chromatin motion patterns during the interphase?

To examine this possibility, we performed 3D telomere tracking in a mutant cell line with double knockout of Lamin A, MEF LmnaKO, and compared the results to the normal cell line (MEF 3T3). Interestingly, the

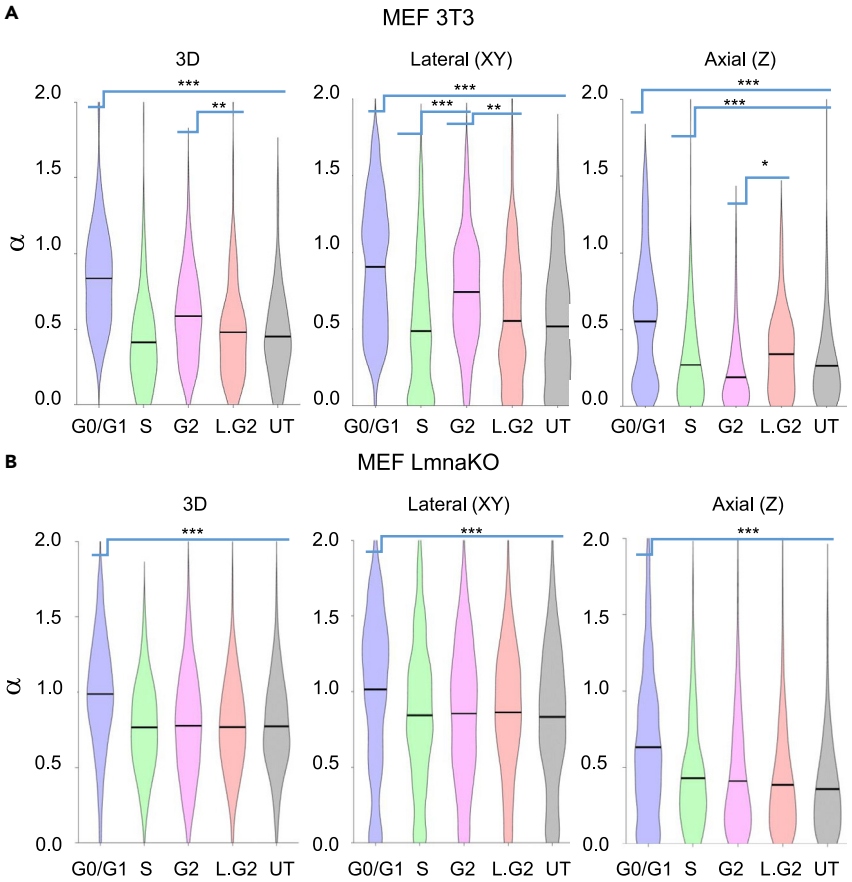

Figure 3. Axial vs lateral analysis and comparison between MEF 3T3 and LmnaKO

(A and B) Anomalous exponent (α) violin plots for the longer time intervals in MEF 3T3 (A) and LmnaKO (B), see also Figure S3 for synchronization validation, and Table S2 for statistical parameters. The MSD curves were calculated for three cases: Lateral (2D, x, y), axial (z), and 3D (x, y, z). Confidence in two sample tests (See STAR Methods for details, and also Table S3): *p < 0.05, **p < 0.01, ***p < 0.001.

differences in anomalous diffusion coefficients between the cell cycle phases in the mutant cells were significantly decreased compared to the normal cells; free subdiffusion was detected in all phases, reaching values close to pure Brownian motion ($\alpha \approx 1$) in G0/G1 (Figures 2C and 2D). This observation is consistent with an earlier study reporting telomere-free subdiffusion in MEF LmnaKO without synchronization for cell cycle phases (Bronshtein et al., 2015).

Axial and lateral diffusions during the interphase are different

Adherent cells have anisotropic dimensions, namely, stretching much further laterally (xy) than normal to the surface (z). It is therefore not surprising that this inherent anisotropy yields a difference in motion between the lateral and the axial dimensions, which is directly observable by our live 3D imaging method. To explore the contributions of the lateral and axial motions to telomere dynamic constraint, we repeated the ensemble MSD analysis for the lateral and axial coordinates separately (Figures 3 and S2), comparing the constraint levels using the anomalous exponent (α). Overall, throughout interphase, lateral motion appeared less confined than axial motion (Figure 3). With respect to the different cell cycle stages, in both the lateral and axial analyses, G0/G1 presented more free diffusion than other phases. The anomalous exponent of the lateral analysis identified that G0/G1 and G2 had higher values than S and late G2, while G0/G1 presented a higher value compared with G2. Interestingly, the axial analysis presented a different situation: Late G2 presented a higher value than S and G2, in which the axial chromosome movement was extremely constrained (Figure 3A).

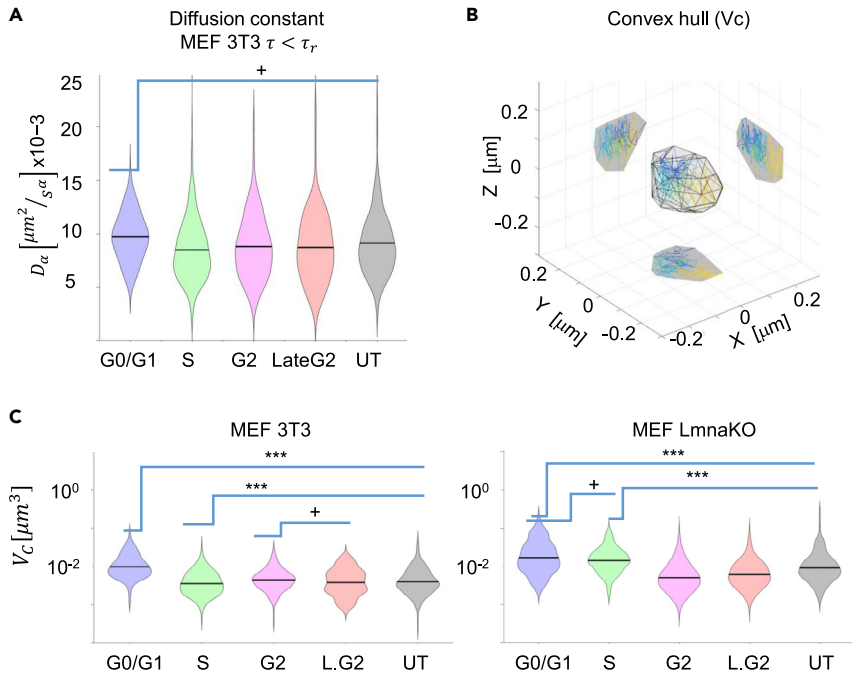

Figure 4. DNA content analysis

(A) diffusion constant D_α for short times ($t<\tau_r$) in MEF 3T3, where α is approximately equal in all phases.

(B) An example of constraining volume calculated by convex hull. 2D projections are shown on the XY, XZ, and YZ planes. The trajectory is color-coded, and the convex hull volume/area is in gray.

(C) Constraining volume distribution, calculated by convex hull at time 25 s (see also other times in Figure S4), for MEF 3T3 (left) and MEF LmnaKO (right). Confidence in two sample tests (See STAR Methods for details): + $p < 0.2$, *$p < 0.05$, **$p < 0.01$, ***$p < 0.001$.

A reasonable explanation for the different constraints between phases is DNA content and chromatin density: increased DNA content should increase the density and decrease the diffusion constant D_α, which is traditionally associated with chromatin condensation (Ma et al., 2019; Shaban et al., 2020). $D_\alpha\left[\mu m^2/s^\alpha\right]$ is dependent on α, and therefore constitutes a good metric for comparison when the different populations have similar mean α. Accordingly, we calculated the diffusion constant from the short interval times linear fit ($\tau < \tau_r$), where the values of α are similar for all the phases, and identified slightly higher value during G0/G1 (Figure 4A), in agreement with the lower expected DNA content levels during G0/G1. We did not calculate D_α for the long interval times ($\tau > \tau_L$), because the α values vary between the phases. Instead, we compared the constraining volumes (V_c), namely the volumes explored by the telomeres within 25 s, for the 3D trajectories (Figure 4C), using convex hull analysis (Figure 4B, see STAR Methods for more details). This analysis revealed a similar picture to the one provided by D_α for the short time intervals (Figure 4A).

In the axial motion, for both the wild-type and lamin A KO cells, the constraint increased from G0/G1 to the S phase and was maximal in early G2 (Figure 3 A). This possibly implies an effect of the amount of DNA on chromatin motion: DNA is doubled during the S phase, while the overall size of the nucleus during all interphase remains relatively constant (Walter et al., 2003); hence, diffusion is expected to be more constrained. The less constrained axial motion during the late G2 phase compared with S and early G2 may derive from the condensation of the chromosome as preparation for mitosis, which reaches a maximum during metaphase-anaphase transition (mitosis was not investigated in this research).

The change in DNA content is not sufficient to explain the cell-cycle-dependent local chromatin motion, as evident in the WT lateral diffusion results, which shows relaxation during early G2 compared to the S phase (Figure 3A). A possible explanation for this effect may be chromosome compartmentalization; the dynamic segregation (Bintu et al., 2018) of the chromosome into local domains of different sizes

can vary during the interphase as part of the phase-dependent cell processes. During S phase, the replication of the genome occurs in multiple loci simultaneously, and the chromosome may segregate into smaller domains (Nozaki et al., 2017; Bintu et al., 2018; Ashwin et al., 2019). Our observation of similar constraints during the S and G2 phases in LmnaKO cells (Figure 2D) supports this explanation; nucleoplasm Lamin A is known to be involved in constraining chromatin dynamics and maintaining nucleus compartmentalization, and therefore its absence will affect the process of chromatin segregation into domains (Bronshtein et al., 2015; Nozaki et al., 2017; Karoutas and Akhtar, 2021). To summarize this section, our data generally show that axial and lateral diffusions are different. A reasonable explanation is embedded in cell morphology: in adherent cells, the available space for diffusion is more limited in the axial direction as manifested in generally reduced axial motion in all phases for both cell lines (Figures 3A and 3B).

Ultimately, chromosomal motion dynamics should be interpreted in the context of the cell's behavior. During G0/G1, a cell's resources are mainly invested in growth, maintenance, and performing the various cell-type-dependent cellular function (e.g. fibroblast, epithelium etc.). Most of the transcription occurs during G1 (Humphrey and Brooks, 2005); accordingly, domain repositioning rates are more frequent, and the chromatin motion is less constrained than other phases. During S phase, chromosomal segregation into more compact domains occurs, which is important for replication of the genome (Nagano et al., 2017; Nozaki et al., 2017; Bintu et al., 2018; Ashwin et al., 2019), and therefore the DNA is most constricted. During G2, the cell prepares for mitosis, including transcription of necessary genes and DNA damage repair. That manifests in a slight relaxation in the constraints, however, DNA content is larger than in the G1 phase, thus limiting the available space for diffusion. In late G2, just before the cell enters prophase (mitosis), the chromosome undergoes significant condensation. The local organization (segregation to domains) is preserved during mitosis (Nozaki et al., 2017), and therefore during late G2, more constrained lateral diffusion may reflect proper condensation and segregation during mitosis.

Closing remarks

In the last decade, our understanding of genome organization and compartmentalization has changed dramatically (Maeshima et al., 2020). Chromatin organization has been found to be highly dynamic at multiple scales, with transient domains forming frequently (Bintu et al., 2018). This local reordering is reflected in the large heterogeneity of local chromatin motion. Our results demonstrate that local chromatin constraints are phase dependent. Furthermore, our unique method revealed different behavior of axial and lateral diffusion in adherent cells, which motivates future investigation into the 3D organization of the nucleus, in the context of 3D culture and *in vivo* studies. Under Lamin A depletion, the differences between the cell cycle phases decreased, consistent with Lamin A's function in the preservation of constrained chromatin diffusion and the stability of chromosome segregation to domains. This adds to the growing body of evidence (Johnson et al., 2004; Nitta et al., 2006; Nitta et al., 2007; Hara et al., 2012; Bronshtein et al., 2015; Vivante et al., 2019; Karoutas and Akhtar, 2021) that ties the involvement of Lamin A to premature aging diseases and other diseases involved with major genome organization instability and cell cycle dysregulation.

Limitations of the study

We used a motif-binding protein, hTRF1, fused to an FP - dsRed. This chimeric protein, DsRed-hTRF1, specifically binds the repeated sequences in the telomere, such that an array of FPs is formed on telomere sites, allowing tracking telomeres as single particles. Generally, when using single-particle tracking (SPT) methods, due to high NA, one should consider the strong polarization along the illumination direction. However, in our work, the signal from each telomere originates from a multitude of fluorescent proteins at random orientations aggregated together at high rotational mobility, several microns above the coverslip. Under these circumstances, we do not observe that the polarization of the illumination has a noticeable effect. As mentioned in the text, we did not separate the quiescent population from the G1 cells; one can design an experiment using other synchronization reagents to separate these populations as well. Finally, the more data the better—the more cells, telomeres, and conditions that can be measured, the more the statistical significance of our findings would improve.

STAR★METHODS

Detailed methods are provided in the online version of this paper and include the following:

SUPPLEMENTAL INFORMATION

Supplemental information can be found online at https://doi.org/10.1016/j.isci.2022.104197.

ACKNOWLEDGMENTS

This work was supported by H2020 European Research Council Horizon 2020 (802567) and by the ISRAEL SCIENCE FOUNDATION (grant No. 450/18). We thank Professor Yuval Garini and Dr. Irena Bronshtein for generously giving us the cell lines and plasmid and for fruitful discussions. We thank Dr. Efrat Barak, Yousef Mansour, and Marian Nicola from the Technion's Life Sciences and Engineering infrastructure center for their help with the flow cytometry experiments, and Professor Noam Kaplan for helpful input.

AUTHOR CONTRIBUTIONS

Conceptualization- TN; Methodology – sample preparation- TN; Methodology – optical setup- BF and LEW; Methodology – Localization- TN, EN, and BF; Methodology – trajectory extraction- YN; Methodology – Data analysis- TN; Software- EN, BF, YN, and TN; Writing- TN, OA, and YS; Supervision- OA and YS;

DECLARATION OF INTERESTS

The authors declare no competing interests.

Received: October 10, 2021
Revised: February 2, 2022
Accepted: March 31, 2022
Published: May 20, 2022

REFERENCES

Albiez, H., Cremer, M., Tiberi, C., Vecchio, L., Schermelleh, L., Dittrich, S., Küpper, K., Joffe, B., Thormeyer, T., von Hase, J., et al. (2006). Chromatin domains and the interchromatin compartment form structurally defined and functionally interacting nuclear networks. Chromosome Res. *14*, 707–733. https://doi.org/10.1007/s10577-006-1086-x.

Ashwin, S.S., Nozaki, T., Maeshima, K., and Sasai, M. (2019). Organization of fast and slow chromatin revealed by single-nucleosome dynamics. Proc. Natl. Acad. Sci. U S A *116*, 19939–19944. https://doi.org/10.1073/pnas.1907342116.

Backer, A.S., and Moerner, W.E. (2014). Extending single-molecule microscopy using optical fourier processing. J. Phys. Chem. B *118*, 8313–8329. https://doi.org/10.1021/jp501778z.

Banani, S.F., Lee, H.O., Hyman, A.A., and Rosen, M.K. (2017). Biomolecular condensates: organizers of cellular biochemistry. Nat. Rev. Mol. Cell Biol. *18*, 285–298. https://doi.org/10.1038/nrm.2017.7.

Bintu, B., Mateo, L.J., Su, J.H., Sinnott-Armstrong, N.A., Parker, M., Kinrot, S., Yamaya, K., Boettiger, A.N., and Zhuang, X. (2018). Super-resolution chromatin tracing reveals domains and cooperative interactions in single cells. Science *362*, eaau1783. https://doi.org/10.1126/science.aau1783.

Bouchaud, J.P., and Georges, A. (1990). Anomalous diffusion in disordered media: statistical mechanisms, models and physical applications. Phys. Rep. *195*, 127–293. https://doi.org/10.1016/0370-1573(90)90099-N.

Bradski, G. (2000). The OpenCV Library. Dr Dobb'S J. Soft. Tools *120*, 122–125.

Breunig, M.M., Kriegel, H.P., Yan Ng, R.T., and Sander, J. (2000). LOF: identifying density-based local outliers. In Proceedings of the 2000 ACM SIGMOD International Conference on Management of Data, pp. 93–104.

Briels, W.,J. (1998). Theory of polymer dynamics. https://cbp.tnw.utwente.nl/PolymeerDictaat/index.html.

Bronshtein, I., Kepten, E., Kanter, I., Berezin, S., Lindner, M., Redwood, A.B., Mai, S., Gonzalo, S., Foisner, R., Shav-Tal, Y., and Garini, Y. (2015). Loss of lamin A function increases chromatin dynamics in the nuclear interior. Nat. Commun. *6*, 8044. https://doi.org/10.1038/ncomms9044.

Bronstein, I., Israel, Y., Kepten, E., Mai, S., Shav-Tal, Y., Barkai, E., and Garini, Y. (2009). Transient anomalous diffusion of telomeres in the nucleus of mammalian cells. Phys. Rev. Lett. *103*, 018102. https://doi.org/10.1103/PhysRevLett.103.018102.

Bui, M., Dimitriadis, E.K., Hoischen, C., An, E., Quénet, D., Giebe, S., Nita-Lazar, A., Diekmann,

S., and Dalal, Y. (2012). Cell-cycle-dependent structural transitions in the human CENP-A nucleosome in vivo. Cell *150*, 317–326. https://doi.org/10.1016/j.cell.2012.05.035.

Cai, S., Chen, C., Tan, Z.Y., Huang, Y., Shi, J., and Gan, L. (2018). Cryo-ET reveals the macromolecular reorganization of S. pombe mitotic chromosomes in vivo. Proc. Natl. Acad. Sci. U S A. *115*, 10977–10982. https://doi.org/10.1073/pnas.1720476115.

Cho, S., Vashisth, M., Abbas, A., Majkut, S., Vogel, K., Xia, Y., Ivanovska, I.L., Irianto, J., Tewari, M., Zhu, K., et al. (2019). Mechanosensing by the lamina protects against nuclear rupture, DNA damage, and cell-cycle arrest. Dev. Cell *49*, 920–935.e5. https://doi.org/10.1016/j.devcel.2019.04.020.

Chowdhary, S., Kainth, A.S., Pincus, D., and Gross, D.S. (2019). Heat shock factor 1 drives intergenic association of its target gene loci upon heat shock. Cell Rep *26*, 18–28.e5. https://doi.org/10.1016/j.celrep.2018.12.034.

Chuang, C.H., Carpenter, A.E., Fuchsova, B., Johnson, T., de Lanerolle, P., and Belmont, A.S. (2006). Long-range directional movement of an interphase chromosome site. Curr. Biol. *16*, 825–831. https://doi.org/10.1016/j.cub.2006.03.059.

Cisse, I.I., Izeddin, I., Causse, S.Z., Boudarene, L., Senecal, A., Muresan, L., Dugast-Darzacq, C., Hajj, B., Dahan, M., and Darzacq, X. (2013). Real-time dynamics of RNA polymerase II clustering in live human cells. Science *341*, 664–667.

Darzynkiewicz, Z., Gong, J., Juan, G., Ardelt, B., and Traganos, F. (1996). Cytometry of cyclin proteins. Cytometry *25*, 1–13. https://doi.org/10.1002/(SICI)1097-0320(19960901)25:1<1::AID-CYTO1>3.0.CO;2-N.

Dechat, T., Shimi, T., Adam, S.A., Rusinol, A.E., Andres, D.A., Spielmann, H.P., Sinensky, M.S., and Goldman, R.D. (2007). Alterations in mitosis and cell cycle progression caused by a mutant Lamin A known to accelerate human aging. Proc. Natl. Acad. Sci. U S A. *104*, 4955–4960. https://doi.org/10.1073/pnas.0700854104.

Von Diezmann, A., Shechtman, Y., and Moerner, W.E. (2017). Three-dimensional localization of single molecules for super-resolution imaging and single-particle tracking. Chem. Rev. *117*, 7244–7275. https://doi.org/10.1021/acs.chemrev.6b00629.

Eltsov, M., Maclellan, K.M., Maeshima, K., Frangakis, A.S., and Dubochet, J. (2008). Analysis of cryo-electron microscopy images does not support the existence of 30-nm chromatin fibers in mitotic chromosomes in situ. Proc. Natl. Acad. Sci. U S A. *105*, 19732–19737. https://doi.org/10.1073/pnas.0810057105.

Ester, M., Kriegel, H.P., Sander, J., and Xu, X. (1996). A density-based algorithm for discovering clusters in large spatial databases with noise. In Proceedings of the 2nd International Conference on Knowledge Discovery and Data Mining (AAAI Press), pp. 226–231.

Fasciani, A., D'Annunzio, S., Poli, V., Fagnocchi, L., Beyes, S., Michelatti, D., Corazza, F., Antonelli, L., Gregoretti, F., Oliva, G., et al. (2020). MLL4-associated condensates counterbalance polycomb-mediated nuclear mechanical stress in Kabuki syndrome. Nat. Genet. *52*, 1397–1411. https://doi.org/10.1038/s41588-020-00724-8.

Ferdman, B., Nehme, E., Weiss, L.E., Orange, R., Alalouf, O., and Shechtman, Y. (2020). VIPR: vectorial implementation of phase retrieval for fast and accurate microscopic pixel-wise pupil estimation. Opt. Express *28*, 10179–10198. https://doi.org/10.1364/OE.388248.

Furlong, E.E.M., and Levine, M. (2018). Developmental enhancers and chromosome topology. Science *361*, 1341–1345. https://doi.org/10.1126/science.aau0320.

De Gennes, P.G. (1971). Reptation of a polymer chain in the presence of fixed obstacles. J. Chem. Phys. *55*, 572–579. https://doi.org/10.1063/1.1675789.

Ghosh, S., and Zhou, Z. (2014). Genetics of aging, progeria and lamin disorders. Curr. Opin. Genet. Dev. *26*, 41–46. https://doi.org/10.1016/j.gde.2014.05.003.

Gibson, B.A., Doolittle, L.K., Schneider, M.W.G., Jensen, L.E., Gamarra, N., Henry, L., Gerlich, D.W., Redding, S., and Rosen, M.K. (2019). Organization of chromatin by Intrinsic and regulated phase separation. Cell *179*, 470–484.e21. https://doi.org/10.1016/j.cell.2019.08.037.

Grigoryan, A., Guidi, N., Senger, K., Liehr, T., Soller, K., Marka, G., Vollmer, A., Markaki, Y., Leonhardt, H., Buske, C., et al. (2018). LaminA/C regulates epigenetic and chromatin architecture changes upon aging of hematopoietic stem cells. Genome Biol. *19*, 189. https://doi.org/10.1186/s13059-018-1557-3.

Hahn, A.T., Jones, J.T., and Meyer, T. (2009). Quantitative analysis of cell cycle phase durations and PC12 differentiation using fluorescent biosensors. Cell Cycle *8*, 1044–1052. https://doi.org/10.4161/cc.8.7.8042.

Hara, K., Ueda, S., Ohno, Y., Tanaka, T., Yagi, H., Okazaki, S., Kawahara, R., Masayuki, T., Enomoto, T., Hashimoto, Y., et al. (2012). NIH3T3 cells overexpressing CD98 heavy chain resist early G1 arrest and apoptosis induced by serum starvation. Cancer Sci. *103*, 1460–1466. https://doi.org/10.1111/j.1349-7006.2012.02304.x.

Hinz, M., Krappmann, D., Eichten, A., Heder, A., Scheidereit, C., and Strauss, M. (1999). NF-kappaB function in growth control: regulation of cyclin D1 expression and G0/G1-to-S-phase transition. Mol. Cell Biol *19*, 2690–2698. https://doi.org/10.1128/mcb.19.4.2690.

Hsieh, T.H.S., Weiner, A., Lajoie, B., Dekker, J., Friedman, N., and Rando, O.J. (2015). Mapping nucleosome resolution chromosome folding in yeast by micro-C. Cell *162*, 108–119. https://doi.org/10.1016/j.cell.2015.05.048.

Humphrey, T., and Brooks, G. (2005). In Methods in molecular biology - cell cycle control, J.M. Walker, ed. (Humana Press), pp. 157–165.

Johnson, B.R., Nitta, R.T., Frock, R.L., Mounkes, L., Barbie, D.A., Stewart, C.L., Harlow, E., and Kennedy, B.K. (2004). A-type lamins regulate retinoblastoma protein function by promoting subnuclear localization and preventing proteasomal degradation. Proc. Natl. Acad. Sci. U S A. *101*, 9677–9682. https://doi.org/10.1073/pnas.0403250101.

Jones, Z.W., Leander, R., Quaranta, V., Harris, L.A., and Tyson, D.R. (2018). A drift-diffusion checkpoint model predicts a highly variable and growth-factor-sensitive portion of the cell cycle G1 phase. PLoS One *13*, e0192087. https://doi.org/10.1371/journal.pone.0192087.

Karoutas, A., and Akhtar, A. (2021). Functional mechanisms and abnormalities of the nuclear lamina. Nat. Cell Biol *23*, 116–126. https://doi.org/10.1038/s41556-020-00630-5.

Kepten, E., Weron, A., Sikora, G., Burnecki, K., and Garini, Y. (2015). Guidelines for the fitting of anomalous diffusion mean square displacement graphs from single particle tracking experiments. PLoS ONE *10*, e0117722. https://doi.org/10.1371/journal.pone.0117722.

Kepten, E., Bronshtein, I., and Garini, Y. (2013). Improved estimation of anomalous diffusion exponents in single-particle tracking experiments. Phys. Rev. E Stat. Nonlin Soft Matter Phys. *87*, 052713. https://doi.org/10.1103/PhysRevE.87.052713.

Kim, J., and Kingston, R.E. (2020). The CBX family of proteins in transcriptional repression and memory. J. Biosci. *45*, 16. https://doi.org/10.1007/s12038-019-9972-5.

Lanni, J.S., and Jacks, T. (1998). Characterization of the p53-dependent postmitotic checkpoint following spindle disruption. Mol. Cell Biol *18*, 1055–1064. https://doi.org/10.1128/MCB.18.2.1055.

Lee, Y.C.G., Ogiyama, Y., Martins, N.M.C., Beliveau, B.J., Acevedo, D., Wu, C.T., Cavalli, G., and Karpen, G.H. (2020). Pericentromeric heterochromatin is hierarchically organized and spatially contacts H3K9me2 islands in euchromatin. PLoS Genet. *16*, e1008673. https://doi.org/10.1371/journal.pgen.1008673.

Levi, V., Ruan, Q., Plutz, M., Belmont, A.S., and Gratton, E. (2005). Chromatin dynamics in interphase cells revealed by tracking in a two-photon excitation microscope. Biophys. J. *89*, 4275–4285. https://doi.org/10.1529/biophysj.105.066670.

Lieberman-Aiden, E., van Berkum, N.L., Williams, L., Imakaev, M., Ragoczy, T., Telling, A., Amit, I., Lajoie, B.R., Sabo, P.J., Dorschner, M.O., et al. (2009). Comprehensive mapping of long-range interactions reveals folding principles of the human genome. Science *326*, 289–293. https://doi.org/10.1126/science.1181369.Comprehensive.

Lin, X., Qi, Y., Latham, A.P., and Zhang, B. (2021). Multiscale modeling of genome organization with maximum entropy optimization. J. Chem. Phys. *155*, 010901. https://doi.org/10.1063/5.0044150.

Liu, N.Q., Maresca, M., van den Brand, T., Braccioli, L., Schijns, M.M.G.A., Teunissen, H., Bruneau, B.G., Nora, E.P., and de Wit, E. (2021). WAPL maintains a cohesin loading cycle to preserve cell-type-specific distal gene regulation. Nat. Genet. *53*, 100–109. https://doi.org/10.1038/s41588-020-00744-4.

Lowe, D.G. (1999). Object recognition from local scale-invariant features. Proc. IEEE Int. Conf. Computer Vis. *2*, 1150–1157. https://doi.org/10.1109/iccv.1999.790410.

Ma, H., Tu, L.C., Chung, Y.C., Naseri, A., Grunwald, D., Zhang, S., and Pederson, T. (2019). Cell cycle- and genomic distance-dependent dynamics of a discrete chromosomal region. J. Cell Biol *218*, 1467–1477. https://doi.org/10.1083/jcb.201807162.

Maeshima, K., Tamura, S., Hansen, J.C., and Itoh, Y. (2020). Fluid-like chromatin: toward understanding the real chromatin organization present in the cell. Curr. Opin. Cell Biol *64*, 77–89. https://doi.org/10.1016/j.ceb.2020.02.016.

Michalet, X., and Berglund, A.J. (2012). Optimal diffusion coefficient estimation in single-particle tracking. Phys. Rev. E Stat. Nonlin Soft Matter Phys. *85*, 061916. https://doi.org/10.1103/PhysRevE.85.061916.

Nagano, T., Lubling, Y., Várnai, C., Dudley, C., Leung, W., Baran, Y., Mendelson Cohen, N., Wingett, S., Fraser, P., and Tanay, A. (2017). Cell-cycle dynamics of chromosomal organization at single-cell resolution. Nature *547*, 61–67. https://doi.org/10.1038/nature23001.

Narendra, V., Rocha, P.P., An, D., Raviram, R., Skok, J.A., Mazzoni, E.O., and Reinberg, D. (2015). CTCF establishes discrete functional chromatin domains at the Hox clusters during differentiation. Science *347*, 1017–1021. https://doi.org/10.1126/science.1262088.

Nehme, E., Freedman, D., Gordon, R., Ferdman, B., Weiss, L.E., Alalouf, O., Naor, T., Orange, R., Michaeli, T., and Shechtman, Y. (2020). DeepSTORM3D: dense 3D localization microscopy and PSF design by deep learning. Nat. Methods *17*, 734–740. https://doi.org/10.1038/s41592-020-0853-5.

Nishino, Y., Eltsov, M., Joti, Y., Ito, K., Takata, H., Takahashi, Y., Hihara, S., Frangakis, A.S., Imamoto, N., Ishikawa, T., and Maeshima, K. (2012). Human mitotic chromosomes consist predominantly of irregularly folded nucleosome fibres without a 30-nm chromatin structure. EMBO J. *31*, 1644–1653. https://doi.org/10.1038/emboj.2012.35.

Nitta, R.T., Jameson, S.A., Kudlow, B.A., Conlan, L.A., and Kennedy, B.K. (2006). Stabilization of the retinoblastoma protein by A-type nuclear lamins is required for INK4A-mediated cell cycle arrest. Mol. Cell Biol *26*, 5360–5372. https://doi.org/10.1128/mcb.02464-05.

Nitta, R.T., Smith, C.L., and Kennedy, B.K. (2007). Evidence that proteasome-dependent degradation of the retinoblastoma protein in cells lacking A-type lamins occurs independently of gankyrin and MDM2. PLoS ONE *2*, e963. https://doi.org/10.1371/journal.pone.0000963.

Nozaki, T., Imai, R., Tanbo, M., Nagashima, R., Tamura, S., Tani, T., Joti, Y., Tomita, M., Hibino, K., Kanemaki, M.T., et al. (2017). Dynamic organization of chromatin domains revealed by super-resolution live-cell imaging. Mol. Cell *67*, 282–293.e7. https://doi.org/10.1016/j.molcel.2017.06.018.

Ohno, M., Ando, T., Priest, D.G., Kumar, V., Yoshida, Y., and Taniguchi, Y. (2019). Sub-nucleosomal genome structure reveals distinct nucleosome folding motifs. Cell *176*, 520–534.e25. https://doi.org/10.1016/j.cell.2018.12.014.

Oshima, J., Risques, R.A., Martin, G.M., Rabinovitch, P.S., and Oshima, J. (2007). Accelerated telomere shortening and replicative senescence in human fibroblasts overexpressing mutant and wild-type lamin A. Exp. Cell Res. *314*, 82–91. https://doi.org/10.1016/j.yexcr.2007.08.004.

Pagano, M. (1996). In Cell Cycle — Materials and Methods, springer, M. Pagano, ed. (Springer Berlin Heidelberg), pp. 65–70.

Pavani, S.R., Thompson, M.A., Biteen, J.S., Lord, S.J., Liu, N., Twieg, R.J., Piestun, R., and Moerner, W.E. (2009). Three-dimensional, single-molecule fluorescence imaging beyond the diffraction limit by using a double-helix point spread function. Proc. Natl. Acad. Sci. U S A. *106*, 2995–2999. https://doi.org/10.1073/pnas.0900245106.

Peddibhotla, S., Lam, M.H., Gonzalez-Rimbau, M., and Rosen, J.M. (2009). The DNA-damage effector checkpoint kinase 1 is essential for chromosome segregation and cytokinesis. Proc. Natl. Acad. Sci. U S A. *106*, 5159–5164. https://doi.org/10.1073/pnas.0806671106.

Pedregosa, F., Varoquaux, G., Gramfort, A., Michel, V., Grisel, O., Blondel, M., Prettenhofer, P., Weiss, R., Dubourg, V., and Vanderplas, J. (2011). Scikit-learn: machine learning in {P}ython. J. Machine Learn. Res. *12*, 2825–2830.

Raz, V., Vermolen, B.J., Garini, Y., Onderwater, J.J., Mommaas-Kienhuis, M.A., Koster, A.J., Young, I.T., Tanke, H., and Dirks, R.W. (2008). The nuclear lamina promotes telomere aggregation and centromere peripheral localization during senescence of human mesenchymal stem cells. J. Cell Sci *121*, 4018–4028. https://doi.org/10.1242/jcs.034876.

Ricci, M.A., Manzo, C., García-Parajo, M.F., Lakadamyali, M., and Cosma, M.P. (2015). Chromatin fibers are formed by heterogeneous groups of nucleosomes in vivo. Cell *160*, 1145–1158. https://doi.org/10.1016/j.cell.2015.01.054.

Sanborn, A.L., Rao, S.S., Huang, S.C., Durand, N.C., Huntley, M.H., Jewett, A.I., Bochkov, I.D., Chinnappan, D., Cutkosky, A., Li, J., et al. (2015). Chromatin extrusion explains key features of loop and domain formation in wild-type and engineered genomes. Proc. Natl. Acad. Sci. U S A. *112*, E6456–E6465. https://doi.org/10.1073/pnas.1518552112.

Sanulli, S., Trnka, M.J., Dharmarajan, V., Tibble, R.W., Pascal, B.D., Burlingame, A.L., Griffin, P.R., Gross, J.D., and Narlikar, G.J. (2019). HP1 reshapes nucleosome core to promote phase separation of heterochromatin. Nature *575*, 390–394. https://doi.org/10.1038/s41586-019-1669-2.

Scaffidi, P., and Misteli, T. (2006). Lamin A-dependent nuclear defects in human aging. Science *312*, 1059–1063. https://doi.org/10.1126/science.1127168.

Shaban, H.A., Barth, R., Recoules, L., and Bystricky, K. (2020). Hi-D: nanoscale mapping of nuclear dynamics in single living cells. Genome Biol. *21*, 95. https://doi.org/10.1186/s13059-020-02002-6.

Shachar, S., Voss, T.C., Pegoraro, G., Sciascia, N., and Misteli, T. (2015). Identification of gene positioning factors using high-throughput imaging mapping. Cell *162*, 911–923. https://doi.org/10.1016/j.cell.2015.07.035.

Shechtman, Y., Weiss, L.E., Backer, A.S., Sahl, S.J., and Moerner, W.E. (2015). Precise three-dimensional scan-free multiple-particle tracking over large axial ranges with tetrapod point spread functions. Nano Lett. *15*, 4194–4199. https://doi.org/10.1021/acs.nanolett.5b01396.

Shechtman, Y., Gustavsson, A.K., Petrov, P.N., Dultz, E., Lee, M.Y., Weis, K., and Moerner, W.E. (2017). Observation of live chromatin dynamics in cells via 3D localization microscopy using tetrapod point spread functions. Biomed. Opt. Express *8*, 5735–5748. https://doi.org/10.1364/BOE.8.005735.

Da Silva-álvarez, S., and Collado, M. (2018). Cellular Quiescence, Encyclopedia of Cell Biology. In Methods in Molecular Biology, H.D. Lacorazza, ed. (Springer New York), pp. 1–5.

Strom, A.R., Emelyanov, A.V., Mir, M., Fyodorov, D.V., Darzacq, X., and Karpen, G.H. (2017). Phase separation drives heterochromatin domain formation. Nature *547*, 241–245. https://doi.org/10.1038/nature22989.

Sullivan, T., Escalante-Alcalde, D., Bhatt, H., Anver, M., Bhat, N., Nagashima, K., Stewart, C.L., and Burke, B. (1999). Loss of A-type lamin expression compromises nuclear envelope integrity leading to muscular dystrophy. J. Cell Biol *147*, 913–920. https://doi.org/10.1083/jcb.147.5.913.

Vivante, A., Brozgol, E., Bronshtein, I., Levi, V., and Garini, Y. (2019). Chromatin dynamics governed by a set of nuclear structural proteins. Genes Chromosomes Cancer *58*, 437–451. https://doi.org/10.1002/gcc.22719.

Walter, J., Schermelleh, L., Cremer, M., Tashiro, S., and Cremer, T. (2003). Chromosome order in HeLa cells changes during mitosis and early G1, but is stably maintained during subsequent interphase stages. J. Cell Biol *160*, 685–697. https://doi.org/10.1083/jcb.200211103.

Weiss, L.E., Naor, T., and Shechtman, Y. (2018). Observing DNA in live cells. Biochem. Soc. Trans. *46*, 729–740. https://doi.org/10.1042/BST20170301.

STAR★METHODS

KEY RESOURCES TABLE

REAGENT or RESOURCE	SOURCE	IDENTIFIER
Antibodies		
Rabbit monoclonal IgG Recombinant Anti-Cyclin D1	Abcam, Cambridge, United Kingdom	Cat# ab16663
Rabbit monoclonal Anti-Cyclin B1	Abcam, Cambridge, United Kingdom	Cat# ab181593
Goat Anti-Rabbit IgG H&L (Alexa Fluor® 488)	Abcam, Cambridge, United Kingdom	Cat# ab150081
Chemicals, peptides, and recombinant proteins		
FluoSpheres 0.04µm 561\605nm	Termo-fisher Scientific: Invitrogen, Waltham, Massachusetts, USA	Cat# F10720
Nocodazole	Termo-fisher Scientific: Acros organic, Fair Lawn, New Jersey, USA	Cat# 358240100
Thymidine	Termo-fisher Scientific: Acros organic, Fair Lawn, New Jersey, USA	Cat# 226740050
Colcemid™ solution	Merck group: Sigma-Aldrich, St. Louis, Missouri, USA	Cat# D1925-20ML
Critical commercial assays		
Lipofectamine® 3000 Transfection Reagent/0.75mL	Termo-fisher Scientific: Invitrogen, Waltham, Massachusetts, USA	Cat# L3000008
FxCycle™ PI/RNase Staining Solution	Termo-fisher Scientific: Invitrogen, Waltham, Massachusetts, USA	Cat# F10797
MycoBlue Mycoplasma Detetector	Vazyme biotech, Nanjing, China	Cat# D101
NucleoSpin® Plasmid miniprep	Macherey Nagel, Düren, Germany	Cat# MAN-740727.250
Experimental models: Cell lines		
Mouse: Mouse Embryonic Fibroblast (MEF 3T3)	Gift from Y. Garini Lab Sullivan et al., (1999)	https://doi.org/10.1083/jcb.147.5.913
Mouse: MEF 3T3 LmnaKO	Gift from Y. Garini Lab Sullivan et al., (1999)	https://doi.org/10.1083/jcb.147.5.913
Recombinant DNA		
DsRed-hTRF1	Gift from Y. Garini Lab Raz et al., (2008)	https://doi.org/10.1242/jcs.034876
Software and algorithms		
Python package: DeepStorm3D	Nehme et al., 2020	https://github.com/EliasNehme/DeepSTORM3D
MATLAB package: VIPR algorithm	Ferdman et al., (2020)	https://github.com/Borisfer/VIPR-Vectorial-Phase-Retrieval-for-microscopy
MATLAB package: CCCDO: Cell-Cycle-Chromatin-Dynamic-Organization	This article	https://github.com/Talns/CCCDO
Python code: Trajectories extraction	This article	https://github.com/yevgenin/CCCDOTrajectories
FlowJo™ v10.7	BD, Franklin Lakes, New Jersey, USA	LS&E-ISU lokey center purchased license
BD FACSDiVa™ Software Version 6.1	BD, Franklin Lakes, New Jersey, USA	LS&E-ISU lokey center purchased license
NIS-Elements	Nikon, Minato City, Tokyo, Japan	Shechtman Lab purchased license

(*Continued on next page*)

Continued

REAGENT or RESOURCE	SOURCE	IDENTIFIER
Other		
Eclipse Ti2-E inverted fluorescent microscope	Nikon, Minato City, Tokyo, Japan	Eclipse Ti2-E
SR HP Apo TIRF ×100/1.49 NA	Nikon, Minato City, Tokyo, Japan	MRD01995
PLUTO-Vis-020 Spatial Light Modulator	Holoeye Photonics AG, Berlin, Germany	PLUTO-Vis-020
PRIME 95B sCMOS camera	Teledyne Photometrics, Tucson, Arizona, USA	PRIME 95B
iChrome MLE laser box: 405,488,561,640	Toptica Photonics, Munich, Germany	iChrome CLE
617/73 nm BrightLine® single-band bandpass filter	Semrock, Rochester, New York 14,586, USA	FF02-617/73-25
Laser quad bandpass filters set	Chroma Technology Corp., Bellows Falls, VT 05101, USA	Chroma TRF 89902-NK

RESOURCE AVAILABILITY

Lead contact

Further information and requests should be directed to and will be fulfilled by the lead contact, Yoav Shechtman (yoavsh@technion.ac.il).

Materials availability

This study did not generate new unique reagents.

Data and code availability

- All data reported in this paper will be shared by the Lead contact upon request.
- All original code has been deposited at GitHub and is publicly available as of the date of publication. DOIs are listed in the Key resources table.
- Any additional information required to reanalyze the data reported in this paper is available from the Lead contact upon request.

EXPERIMENTAL MODEL AND SUBJECT DETAILS

Mouse embryonic fibroblast (MEF 3T3) and MEF 3T3 double Lamin-A KO cell lines were kindly given by Yuval Garini's lab (Bronshtein et al., 2015); Both cell lines, MEF 3T3 and MEF 3T3 double Lamin-A KO were originally generated by Sullivan (Sullivan et al., 1999) from 13-day-old mice embryos (Information regarding the cell's sex was not reported). The absence of Lamin-A was validated by a Lamin-A containing plasmid inserted into the KO cell line which reconstituted wild-type behavior (Bronshtein et al., 2015), and also by lack of immunofluorescence signal as measured by microscopy, compared to the wild-type (unpublished). Both cell lines were tested by us to be mycoplasma-free, using the MycoBlue mycoplasma detector (Vazyme biotech, D101).

METHOD DETAILS

Experimental procedures

Calibration bead sample for phase retrieval

1% Polyvinyl alcohol (PVA) solution was made by dissolving 1 gr PVA powder (Sigma-Aldrich, 341584) in 100mL double distilled water, and mild heating for 24 h. 0.04 μm FluoSphere 605 nm stock solution (Termo-fisher, F10720) was diluted 10^{-6} in 1% PVA. 10 μL of the diluted solution was spread on a glass-bottom culture plate (NEST scientific, 801002) homogenously, using a homemade spin-coater, and dried in a chemical hood.

Live cell sample preparation

MEF 3T3 and MEF 3T3 LmnaKO cells (gift from Y. Garini's lab (Sullivan et al., 1999)) were grown for two weeks (four passages) in complete medium containing DMEM-Ham's/F12 (Biological industries,

01-170-1A), supplemented with 10% FBS (Biological industries, 04-007-1A), 1% L-glutamine solution (Biological industries, 03-020-1B) and 1% Penicillin-Streptomycin Solution (Biological industries, 03-031-1B), in a 37°C, 5% CO_2 incubator, to allow stable cell cycle. Both cell lines were tested to be mycoplasma-free, using the MycoBlue mycoplasma detector (Vazyme biotech, D101). For each imaging session, two samples were prepared: one for imaging and one for flow cytometry analysis. For imaging samples only, cells were transfected using lipofectamine 3000 (Termo-fisher, L3000008): 10 μg DsRed-hTRF1 plasmid (gift from Y. Garini lab (Raz et al., 2008)) was mixed with 20 μL P3000 reagent in 1 mL phenol red-free DMEM-Ham's/F12 (Gibco, Termo-fisher, 11039021); 30 μL Lipofectamine3000 was diluted in 1mL phenol red-free DMEM-Ham's/F12; the DNA mix was added to the Lipofectamine 3000 mix and incubated for 30 min in RT. Cell suspension was adjusted to 7.5×10^5 cells/mL and mixed with the transfection mix to a final volume of 10 mL. The cells were then plated in a 75 cm^2 flask and returned to the incubator for 28 h before starting synchronization protocols as described below. The control sample for flow cytometry then underwent the same treatments as the imaging sample, except transfection.

Cell cycle phase synchronization

For cell cycle synchronization we utilized a natural regulatory mechanism of the cell cycle-checkpoint activation. By different treatment (see below) cell arrested cell cycle progression by activating a checkpoint, causing enrichment of cell population at the phase before the activated checkpoint (Humphrey and Brooks, 2005; Da Silva-álvarez and Collado, 2018; Jones et al., 2018). Cells were harvested using Trypsin-EDTA Solution (Biological industries, 03-050-1A), and cell concentration was adjusted to 2×10^6 cells/mL to encourage contact inhibition induced quiescence, due to high cell density. Cells were washed twice (centrifuge at 2200 rpm for 2min) with phosphate buffer saline, PBS (Sigma-Aldrich, 59331C), re-suspended in low serum (0.5%) DMEM-Ham's/F12, plated in a 75 cm^2 flask, and grown for 48 h. After 48 h of growth in a low serum medium, each cell sample was treated differently, according to the specific cell cycle phase synchronization protocol: G0/G1 synchronized cells were left to grow an additional 24 h in a low serum medium; G2 synchronized cells were harvested, concentrated to 7.5×10^5 cells/mL, and re-suspended in a complete medium containing 0.5 μg/mL nocodazole (Acros organics, 358240100), and grown for 48 h; Late G2 synchronized cells were harvested, concentrated to 7.5×10^5 cells/mL, and re-suspended in a complete medium containing 0.04 μg/mL Colcemid (Sigma-Aldrich, D1925), and grown for 48h (note that colcemid induces M checkpoint activation, however, hTRF1 binds less efficiently to telomeres during the M phase, thus cells were considered to be in late G2 rather than M phase).24h before imaging and while synchronizing; cells were plated on glass-bottom culture plates in their synchronization medium. For S enrichment, cells were harvested, washed twice with PBS, concentrated to 2×10^6 cells/mL, re-suspended in a complete medium containing 2 mM thymidine (Acros, 226740050), and grown for 16 h. Cells were washed twice with PBS, concentration adjusted to 7.5×10^5 cells/mL, and allowed to recover for 6–8 h in complete medium on glass-bottom plates (imaging sample) or 25 cm^2 flask (flow cytometry).

Flow cytometry analysis

Flow cytometry analysis was performed to validate cell cycle synchronizations using cyclin level (rectangular gate in Figure S3) and DNA content stains (PI histogram peaks are linear with DNA content (Pagano, 1996), bar gates in Figure S3A), according to several modified protocols (Darzynkiewicz et al., 1996; Pagano, 1996; Lanni and Jacks, 1998; Hinz et al., 1999; Humphrey and Brooks, 2005; Peddibhotla et al., 2009; Da Silva-álvarez and Collado, 2018). Cells were fixed with 4% PFA (Sigma-Aldrich, 158127) solution and stored at 4°C until the analysis day. On the same day of analysis cells were permeabilized with 1% Triton X-100 (Sigma-Aldrich, T8787) for 30 min. The cells were washed twice with PBS and incubated with a primary antibody (either 5.95 [μg/mL] Rabbit monoclonal Anti-Cyclin B1, abcam, ab181593; or 9.7 [μg/mL] Rabbit monoclonal IgG Anti- Cyclin D1, abcam, ab16663) for 1 h in RT. The cells were then incubated for 30 min with ×2000 diluted Goat Anti-Rabbit IgG H&L Alexa Fluor® 488 (abcam, ab150081) on ice. Finely, cells were stained with FxCycle™ PI/RNase Staining Solution (Termo-Fisher scientific, F10797) following manufacturer protocol. Flow cytometry data was collected using a BD LSR-II analyzer operated by FACS-Diva6.1 software, with 488 nm laser, and either 695/40 or 530/30 emission filters for DNA content or Alexa Fluor® 488, respectively. Data were analyzed using FlowJO v10 software.

In the S enrichment experiment we applied S phase gating determined by PI staining of untreated control sample (bar gates in Figure S3A). For the rest of the phases we gated for cyclins by using FMO (fluorescent minus one (Pagano, 1996)) method on PI stain control samples (Figure S3B). Since we have the cyclin profile of MEF 3T3, we used cyclin stains in the WT as a control. MEF 3T3 validation performed as follow: G0/G1

synchronization was determined by PI and cyclin D1 (Figure S3B); G2 and late G2 phases synchronization was determined by PI and elevated level of cyclin B1 (Figures S3C and S3D).

MEF 3T3 and MEF LmnaKO PI histograms in the untreated population were different. The MEF LmnaKO cell PI histogram, unlike MEF 3T3, included a sub-G0/G1 peak, that was negative to Cyclin D1 and implied apoptotic cells (Hara et al., 2012) (Figure S3E). The main peak indicated low levels of Cyclin D1 and middle levels of Cyclin B1, and was thus considered as a "combined phase" G1S for flow cytometry validation (see Table S2). Similar to MEF 3T3, the G2/M cells presented a high level of cyclin B1 and a low level of Cyclin D1 (Figure S3E). Synchronizations of MEF LmnaKO were determined by PI, and elevation of both cyclin D1 and B1 levels (Figures S3E and S3F).

Microscopy

PSF engineering included 4f optical system with an optimized phase mask in the emission path, encoding information of a 4 μm axial (Z) range into the 2D image, such that no scanning was required: the different point spread function (PSF) shapes are proportional to the axial position of the given telomere (Nehme et al., 2020). A detailed illustration of the 4f system is given in Figure S1A. Cells were imaged using an inverted fluorescence microscope (Nikon Eclipse Ti), with a ×100/1.49 NA oil objective (SR HP Apo TIRF ×100/1.49 NA, Nikon MRD01995). Fluorescent excitation was performed with 561 nm laser (iChrome MLE, Toptica Photonics). The emitted light was filtered with 617/72 bandpass filter (Semrock, FF02-617/73-25) and was extended by 4f setup, which included spatial light modulator, SLM (PLUTO-2.1, Holoeye Photonics AG) for phase mask projection of the optimized phase mask (Nehme et al., 2020), Figure S1A. Images were acquired using a sCMOS camera (PRIME 95B, Teledyne Photometrics, Tucson, Arizona, USA). Before each imaging session the following preparations were made: 1. A day before, the microscope incubator cage (OkoLab) was set to 37°C and 5% CO_2; 2. Just before starting live cell imaging, bead calibration sample with water drop for phase retrieval (Ferdman et al., 2020) was imaged with 61 steps of 100nm (z stack), 100mW laser power and exposure time of 300 ms. Live-cell samples were imaged with 10mW laser power and exposure time of 100 ms for 150 s. Automated focusing (Perfect Focus) was active during live cell imaging.

Data analysis and post-processing

Localization by PSF engineering and DeepSTORM3D

To obtain an accurate 3D localization by considering the optical system aberrations, the experimental phase mask was calculated using VIPR algorithm (Ferdman et al., 2020), using the calibration bead sample. The resulting phase mask then was used to train the DeepSTORM3D convolutional-neural-network (CNN) with the specific parameters of each session (see parameters in Table S1). For the live cell data, the emitters in each frame were localized by the trained nets, one cell at each net run (Figure S1B). The bead signal is brighter and less noisy than telomeres in a live cell. We use the bead measurements only for calibration of our system; specifically, for the VIPR algorithm for learning the experimental phase mask, namely the shape of the PSF. However, for actual training of the net, the expected signal is calculated from randomly selected live cell data, which defines the photon count parameters (k,θ), see Table S1.

Nucleus lateral drift compensation

Global motion of the entire nucleus was compensated for, effectively canceled, algorithmically, as follows. For each frame in an acquisition sequence, Scale-invariant feature transform (SIFT) features were used to compute the affine 2D transformation homography matrix relative to the first image in the sequence, using the OpenCV library (Bradski, 2000; Lowe, 1999). Then, the lateral coordinates of the localizations in each frame were transformed using the computed homography matrices, while the axial coordinates were left intact (Figure S1C).

Trajectory reconstruction

After nucleus drift compensation transformation, the whole set of 3D localization points in the image sequence was clustered to trajectories with the DBSCAN (Ester et al., 1996) algorithm, and the points in each cluster were filtered for outliers exclusion, using LOF algorithm (Breunig et al., 2000). Both algorithms were taken from the Scikit-learn (Pedregosa et al., 2011) library. Each separate resulting cluster of points was averaged per frame, resulting in separate trajectories, each having one point per image frame.

Then, the trajectories were filtered by keeping only those which are: a) longer than 50 frames and; b) having an average gap length between consecutive points smaller than 100 frames (Figure S1D).

Mean squared displacement (MSD) analysis

A common method to determine the type of a single particle motion is the time average mean squared displacement (TA-MSD), where the average squared distance that a diffusing particle will travel within a specific time window is calculated (Bouchaud and Georges, 1990). The calculation of MSD is given by (Kepten et al., 2013; Kepten et al., 2015) Equation 1.

Equation 1: Mean square displacement (MSD). $|\vec{r}| = \sqrt{x^2+y^2+z^2}$ is the 3D position vector, $\tau-$ is time interval, given by $\tau = n * \delta t; \delta t-$ is exposure time (frame rate), and N is the total number of time steps.

$$\langle r^2(\tau)\rangle = (N-n)^{-1}\sum_{m=1}^{N-n}[r(m\delta t+\tau) - r(m\delta t)]^2 \qquad \text{(Equation 1)}$$

To identify the type of fractional-Brownian-Motion (fBM) of particle population, power law is applied on MSD, given by (Kepten et al., 2013; Kepten et al., 2015) Equation 2.

Equation 2: fBM MSD power law. $\langle r^2(\tau)\rangle$ is the MSD, α is the anomalous exponent, and $D_\alpha\left[\mu m^2/s^\alpha\right]$ is the anomalous exponent dependant diffusion constant.

$$\langle r^2(\tau)\rangle = D_\alpha \cdot \tau^\alpha \qquad \text{(Equation 2)}$$

Three types of diffusion can be defined by the anomalous exponent (Figure 1C): constrained diffusion (subdiffusion) when $\alpha < 1$; pure Brownian motion when $\alpha = 1$; and super-diffusion (dragging force is imposed) when $\alpha > 1$. To find the value of the anomalous exponent and diffusion constant, a linear fit was obtained by the log of Equation 2 divided by time, given by Equation 3(Bouchaud and Georges, 1990; Kepten et al., 2013; Kepten et al., 2015). First, the transition times were determined for each phase from the ensemble MSD curve (Figure S1E), and then the parameters (α, D_α) were calculated for each time zone and each trajectory. For ensemble MSD analysis the minimal length of a trajectory was set to 150 time points.

Equation 3: the linear form of fBM MSD equation.

$$\log\left(\frac{\langle r^2(\tau)\rangle}{\tau}\right) = (\alpha-1)\log(\tau)+\log(D_\alpha) \qquad \text{(Equation 3)}$$

Determining transition times for MSD analysis

Similarly to the analysis done in (Bronshtein, 2015), we distinguished between two time zones: short-time intervals, $t < \tau_r$, and long-time intervals, $t \in [\tau_L, 30s]$. We determined the transition times from the ensemble MSD curve of each phase separately, then calculated the anomalous exponent for each time zone and for each trajectory separately. The first transition time (τ_r) was defined as the longest time interval such that the ensemble MSD curve linear fit provided $\alpha < 0.25$ with Pearson correlation higher than 0.9. τ_L was defined by the shortest time interval such that the linear fit of the interval $[\tau_L, 30\ s]$ gave a Pearson correlation value higher than 0.9.

Manual validation of each trajectory

We avoided manual analysis as much as possible. However, some trajectories barely passed the automated filtering requirements, for example, by being slightly longer then threshold, containing gaps slightly smaller than threshold or having multiple number of gaps. Therefore, we validated each trajectory manually and excluded only those who clearly cause biased results.

Constraining volume calculation using convex hull

The constraining volume was calculated directly from the trajectory coordinates within 25 s before calculation of the convex hull, outliers were removed using median filter (outlier is a value that is more than three scaled median absolute deviations, MAD). The resulted distributions are presented in Figure 4, main text.

QUANTIFICATION AND STATISTICAL ANALYSIS

Statistical significance test

Two sample t-tests were performed for all distributions; The null hypothesis defined that the two distributions have the same mean, with unknown variance which may be unequal. We did not apply trim or permutations. Since parameters calculated in biological samples may not fit well normal distributions, to further test the statistical significance in this light, we performed a Mann-Whitney non parametric U test and a two-sample Kolmogorov-Smirnov (KS) test, and received similar significances (see Table S3). U test was run using asymptotic method for p-value calculation, when the alternative hypothesis is that the two sample do not have the same distribution. We did not apply continuity correction. KS test was run with the following parameters: The null hypothesis is that the two distributions are identical, under the assumption that the measured values are from continuous distributions. Also for this test we used asymptotic method for p-value calculation. All functions for the statistical tests are from Python SciPy library.

The three tests are mostly consistent (see Table S3). In the figures, we report the strictest result of all three tests per case. The p-value reports whether the null hypothesis was rejected, marked in the figures as follows: * for $p < 0.05$, ** for $p < 0.01$ and *** for $p < 0.001$. All p-values for the anomalous exponent statistical tests are presented in Table S3. For the diffusion constant and constraining volume (Figures 4 and S4) we also included a confidence threshold of 80% and mark it differently (+ for $p < 0.2$).

Estimating localization precision

We calculated axial and lateral localization precision using three different methods: 1. by DeepSTORM3D module (Nehme et al., 2020), which uses the simulated training set to estimate axial and lateral precision (see Table S1); 2. using the ensemble MSD curves, of the axial and lateral analysis separately, to estimate localization error as explained in earlier studies (Michalet and Berglund, 2012; Shechtman et al., 2015). The reduced square localization error (ε) is given by Equation 4:

Equation 4: Reduced squared localization error, ε. σ^2 is the squared static localization error, D_α is the diffusion constant, Δt is the exposure time and R is the motion blur coefficient.

$$\varepsilon = \frac{\sigma^2}{D_\alpha \Delta t} - 2R \qquad \text{(Equation 4)}$$

We calculated σ^2 from the first three time points in the MSD curve, by a linear fit, while σ^2 is the intersection of this line with y axis. The diffusion constant (D_α) was calculated from the 3D analysis, the exposure time was 0.1 s and we ignored motion blur (R = 0).

3. We used the "slowest" telomeres (with very low anomalous exponent) as an approximation for an *in-cellulo* fiducial, and bound the precision by repeatedly localizing them in 3D for all measured time points (up to 1500 frames), and removing a low-order polynomial (degree 5) for canceling slow motion. The resulted values are presented in Table S1. Note that since these telomeres still exhibit some motion, this quantification could be regarded as a 'worst-case' bound on experimental localization precision.

Estimating axial drift compensation

The comparison between the contribution of axial and lateral information (Figures 3A and 3B) implied that 2D analysis provides only partial information on the cell-cycle dependency of local chromatin movements on a genome-wide scale. To validate that compensation of axial drift is not required, we examined all cells with at least 10 detected trajectories and calculated the center of mass (CM) for the Z coordinate only. Next, we fitted a 5^{th} degree polynomial to the CM trajectory (Figure S2B) and subtracted this curve from each trajectory. We find very slight differences between the compensated and not compensated data (Figure S2C). Accordingly, and to avoid the risk of 'over-correction', the analysis presented in the main text includes all cells and trajectories used for the 3D analysis without compensation for axial drift.